JGR Solid Earth

RESEARCH ARTICLE
10.1029/2024JB029824

Electrical Conductivity and Sound Velocities of Talc Under High Pressure and High Temperature Conditions and Application to the Subducting Cocos Plate

Ming Hao[1], Anne Pommier[1], Emmanuel A. Codillo[1], Michael J. Walter[1], Andrew J. Cross[2], Rostislav Hrubiak[3], Lara Wagner[1], Andrew R. Thomson[4,5], Jing Yang[1], and Nicholas Backhouse[4]

[1]Earth and Planets Laboratory, Carnegie Institution for Science, Washington, DC, USA, [2]Department of Geology and Geophysics, Woods Hole Oceanographic Institution, Woods Hole, MA, USA, [3]X-ray Science Division, Argonne National Laboratory, Argonne, IL, USA, [4]Department of Earth Sciences, University College London, London, UK, [5]Department of Earth Sciences, Natural History Museum, London, UK

Abstract Talc is expected to be an important water carrier in Earth's upper mantle, and understanding its electrical and seismic properties under high pressure and temperature conditions is required to detect possible talc-rich regions in subduction zones imaged using geophysical observations. We conducted acoustic and electrical experiments on natural talc aggregates at relevant pressure-temperature conditions. Compressional wave velocity (*Vp*) was measured using ultrasonic interferometry in a Paris-Edinburgh press at pressures up to 3.4 GPa and temperatures up to 873 K. Similar *Vp* values are obtained regardless of the initial crystallographic preferred orientation of the samples, which can be explained by talc grain reorientation during the experiment, with the (001) plane becoming perpendicular to the uniaxial compression axis. Electrical conductivity of the same starting material was determined using impedance spectroscopy in a multi-anvil press up to 6 GPa and 1263 K. Two conductivity jumps are observed, at ~860–1025 K and ~940–1080 K, depending on pressure, and interpreted as talc dehydroxylation and decomposition, respectively. Electrical anisotropy is observed at low temperature and decreases with increasing pressure (~10 at 1.5 GPa and ~2 at 3.5 GPa). Comparison of acoustic and electrical results with geophysical observations in central Mexico supports the presence of a talc-bearing layer atop the subducted Cocos plate.

Plain Language Summary Talc is a mineral that transports water inside the Earth. Understanding its seismic and electrical properties is important to detect its presence at depth and to follow the water cycle. In this study, we measured these two physical properties on a talc rock at relevant temperature and pressure conditions. We observe that the seismic velocities can be >0.8 km/s slower than those reported in previous studies, which is caused by grain reorientation in the high-pressure device. This type of rock deformation can also occur in nature. The electrical response of talc shows two sharp changes at specific temperatures. These changes indicate two transformations in the structure of the mineral. Applied to the field, our experimental findings suggest that a talc-bearing layer under central Mexico can explain the field (seismic and electrical) observations. Our study shows that the combination of different physical properties is important to understand the deep water cycle in our planet.

Key Points:

- Acoustic and electrical measurements were performed on natural talc aggregates at high pressure and temperature conditions
- The experimental data set was complemented with a series of textural and chemical analyses (electron backscatter diffraction (EBSD), electron microprobe analyses, X-ray diffraction, Raman spectroscopy)
- A thin talc-bearing layer can explain the field seismic and electrical observations atop the subducted Cocos plate below central Mexico

Supporting Information:

Supporting Information may be found in the online version of this article.

Correspondence to:

M. Hao and A. Pommier,
mhao@carnegiescience.edu;
apommier@carnegiescience.edu

Citation:

Hao, M., Pommier, A., Codillo, E. A., Walter, M. J., Cross, A. J., Hrubiak, R., et al. (2024). Electrical conductivity and sound velocities of talc under high pressure and high temperature conditions and application to the subducting Cocos plate. *Journal of Geophysical Research: Solid Earth*, *129*, e2024JB029824. https://doi.org/10.1029/2024JB029824

Received 29 JUN 2024
Accepted 8 NOV 2024

Author Contributions:

Conceptualization: Ming Hao, Anne Pommier, Emmanuel A. Codillo, Michael J. Walter, Lara Wagner
Data curation: Ming Hao, Andrew J. Cross
Formal analysis: Ming Hao, Anne Pommier, Jing Yang
Funding acquisition: Anne Pommier
Investigation: Ming Hao, Anne Pommier, Emmanuel A. Codillo
Methodology: Ming Hao, Anne Pommier, Andrew J. Cross, Rostislav Hrubiak, Andrew R. Thomson
Project administration: Anne Pommier
Resources: Anne Pommier, Rostislav Hrubiak

1. Introduction

Water is transported to Earth's deep interior in subducting slabs, where different hydrous minerals are stable at specific depths (e.g., Poli & Schmidt, 2002; Schmidt & Poli, 2013). Knowledge of the physical properties of these minerals, including seismic velocity, and electrical conductivity, is required to understand the deep water cycle and, more generally, the dynamics of subduction zones. Among these hydrous minerals, talc ($Mg_3Si_4O_{10}(OH)_2$) contains 4.5–5 wt.% water and is stable up to 1073 K at 2–3 GPa (e.g., Pawley & Wood, 1995). Talc-rich rocks are thought to form through reactions between ultramafic mantle rocks and silica/CO_2-rich fluids produced by dehydration of the subducting lithosphere (Manning, 1995, 1997). Due to its low frictional strength, talc can localize deformation and influence the seismogenic properties of faults and the slab-mantle interface (Chen et al., 2017; Hirauchi et al., 2020). The presence of mechanically-mixed sediments, mafic, and ultramafic rocks—as well as the likely abundance of silica/CO_2-bearing fluids along the upper slab interface—favors metasomatic talc formation (Manning, 1995). Above its thermal stability limit, talc breaks down to an assemblage of enstatite

Software: Anne Pommier, Andrew J. Cross, Rostislav Hrubiak, Jing Yang
Supervision: Anne Pommier, Michael J. Walter
Validation: Anne Pommier, Michael J. Walter
Visualization: Ming Hao, Anne Pommier, Andrew J. Cross
Writing – original draft: Ming Hao, Anne Pommier
Writing – review & editing: Ming Hao, Anne Pommier, Emmanuel A. Codillo, Michael J. Walter, Andrew J. Cross, Rostislav Hrubiak, Lara Wagner, Andrew R. Thomson, Nicholas Backhouse

and quartz/coesite plus a free fluid phase (Bose & Ganguly, 1995; Pawley & Wood, 1995). It is therefore important to examine the physical properties of talc and its dehydration products for interpreting geophysical observations from the slab-mantle interface region.

From a seismic velocity standpoint, talc is a relatively slow mineral, and its presence has often been suggested as an explanation for low seismic velocities observed at some subduction zones. For example, Kim et al. (2013) and Peng et al. (2022) proposed that talc might explain the ultra-slow velocity layer (USL) detected using seismic receiver functions atop the flat subducted slab beneath central Mexico (Dougherty et al., 2012; Kim et al., 2010; Song et al., 2009), although the layer was not detected in the tomographic study of Espindola-Carmona et al. (2021). If present, this USL was inferred to be 3–5 km thick and with a P-wave velocity (*Vp*) of 5–6 km/s at depths of ∼45–50 km (Kim et al., 2010).

Electromagnetic observations can image the distribution of hydrous phases that form high-conductivity regions in subduction zones (e.g., Egbert et al., 2022; McGary et al., 2014; Pommier & Evans, 2017). Such observations have motivated electrical investigations of several hydrous minerals in the laboratory, including brucite (Guo & Yoshino, 2014), chlorite (Manthilake et al., 2016), amphibole (Hu et al., 2018), lawsonite (Manthilake et al., 2015; Pommier et al., 2019), phengite (Chen et al., 2018), dense hydrous silicates (Guo & Yoshino, 2013), and talc (e.g., Wang & Karato, 2013; Wang et al., 2020). Using electromagnetic measurements across the Trans-Mexican Volcanic Belt (TMVB) where the USL is detected, Jödicke et al. (2006) observed a high-conductivity region located at ∼70 km depth along the subducted plate. Manea and Manea (2011) modeled the thermal structure of the Cocos plate and suggested that the conductivity anomalies observed by Jödicke et al. (2006) are likely related to fluids produced by the dehydration of hydrous minerals. This suggestion was echoed by Kim et al. (2013) who proposed that electrical anomalies in this region could reflect talc dehydration. Indeed, the slab surface temperature is estimated to be ∼1073 K at ∼70 km depth (Syracuse et al., 2010; Manea & Manea, 2011; van Keken and Wilson, 2023a, 2023b), which is similar to the dehydration temperature of talc at this depth (Berman, 1988; Bose & Ganguly, 1995; Pawley & Wood, 1995).

The current data set of the seismic properties of talc is limited and shows contrasting results. Using laboratory experiments at 0.5 GPa, Bailey and Holloway (2000) observed a decrease in *Vp* values from 5.27 to 4.35 km/s as temperature increases from 298 to 1073 K, using an internally heated pressure vessel and with sample thickness measurements before and after the experiment. Using a multi-anvil press at room temperature with in situ measurements of sample thickness, Chen et al. (2023) measured a monotonic increase in *Vp* (up to ∼7 km/s) with increasing pressure to 5.6 GPa, while *Vs* values increase up to 3.2 GPa and then decrease from 3.2 to 5.6 GPa. First principles simulations of talc single crystals were performed previously to calculate the pressure dependence of elastic properties at high pressure and room temperature (Mainprice et al., 2008; Peng et al., 2022; Ulian et al., 2014). However, the previous results from experimental and first principles studies are inconsistent, with reported *Vp* and *Vs* values differing by up to ∼45% and ∼35%, respectively. This discrepancy presents a challenge for interpreting field observations and highlights the need for new acoustic studies in the laboratory. The electrical properties of talc have been measured between 0.5 and 4 GPa and up to 1300 K (Guo et al., 2011; Wang et al., 2020; Wang & Karato, 2013; Zhu et al., 2001). The different electrical data sets show that conductivity increases significantly with temperature by six orders of magnitude from 500 to 1300 K. However, in these previous studies, temperature was increased while the sample undergoes phase transformation (e.g., dehydration). This experimental approach makes it difficult to distinguish between the effect of dehydration and heating on talc conductivity, which requires electrical measurements at fixed temperature.

Here we report new acoustic and electrical measurements on natural polycrystalline talc over a wide range of pressure-temperature conditions relevant to subduction zones. The use of the same starting material for both measurements ensures that electrical and acoustic measurements probe samples with identical starting composition and structure. Velocity measurements were performed using ultrasonic interferometry at 0–3.4 GPa and up to 873 K, while electrical conductivity was measured using impedance spectroscopy at 1.5–6 GPa and up to 1223 K. Our acoustic and electrical results are integrated and compared with geophysical observations of the Cocos plate to evaluate the potential presence of a talc-bearing layer atop the slab beneath central Mexico.

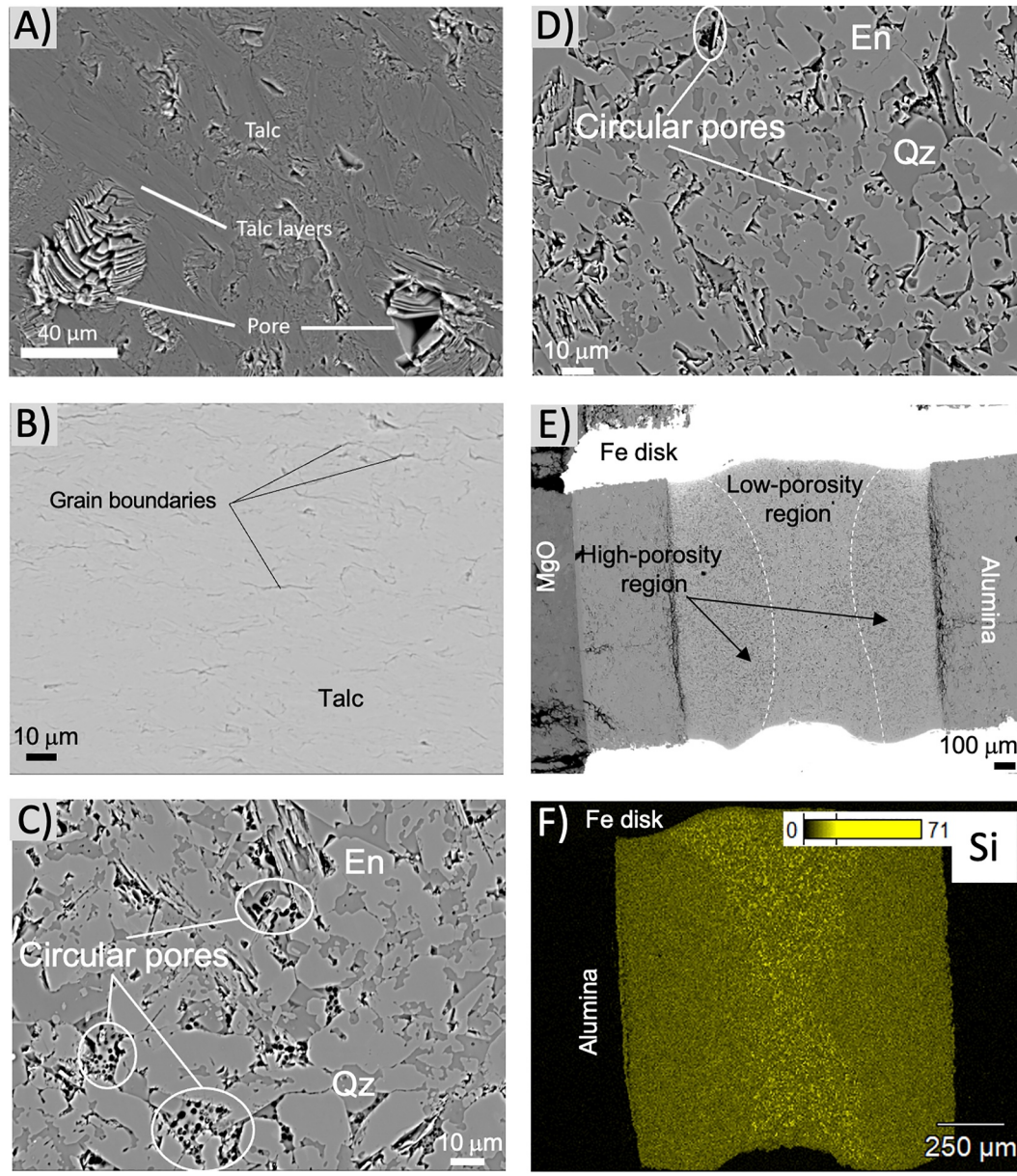

Figure 1. Electron microscopy images of natural talc used in this study. (a) Back-scattered electron (BSE) image of the starting material. (b) BSE image of the retrieved sample from acoustic experiment A1. (c) BSE image of sample from electrical experiment BBC47 (quenched at 1223 K and 1.5 GPa), showing the breakdown products of talc (enstatite (En) and quartz (Qz) grains), as well as areas of high porosity. (d) BSE image of sample from electrical experiment BBC46 (quenched at 1263 K and 1.5 GPa), showing a similar texture to that of sample BBC47 in (c). (e) BSE image of sample BBC47, with Fe electrodes visible at the top and bottom. Porosity is higher in the outer portion of the sample than in the central portion and indicates the presence of fluids. (f) Energy-dispersive spectroscopy (EDS) map for element Si for sample BBC47. The scale bar indicates the number of counts.

2. Methods

2.1. Starting Materials

The starting material is natural, fine-grained talc from Minnesota, USA, that exhibits a strong alignment of (001) cleavage planes (Figure 1a). Based on electron microprobe analyses (Table 1), the chemical formula of the starting talc material is $Na_{0.010(5)}K_{0.001(1)}Mg_{3.02(3)}Fe_{0.026(1)}Ca_{0.018(9)}Al_{0.005(1)}Si_{3.96(2)}O_{10}(OH)_2$, corresponding to a water content of 4.73 (3) wt.%. Both the Archimedes method and X-ray diffraction (XRD) were used to

Table 1
Chemical Composition of the Starting Material Used in This Study and Comparison With Previous Electrical Works

Oxide	Wang et al. (2020)	Guo et al. (2011)	Wang and Karato (2013)	This study
SiO_2	64.3	63.8	62.4	62.9
TiO_2	0.00	0.07	0.01	0.01
Al_2O_3	0.05	0.05	0.10	0.07
Cr_2O_3	0.00	0.00	0.08	0.01
FeO	0.81	0.37	0.51	0.50
MnO	0.01	0.00	0.00	0.00
MgO	30.2	31.0	31.3	32.2
CaO	0.03	0.03	0.08	0.23
Na_2O	0.03	0.00	0.01	0.07
K_2O	0.00	0.00	0.05	0.01
Total	95.4	95.3	94.5	95.9

Note. (In wt.%.; n.d. = Not Determined.)

determine the density of the starting material, yielding 2.72 (1) and 2.75 (3) g/cm^3, respectively. Three types of sample were prepared from the starting material: (a) aggregates cut with the (001) cleavage planes perpendicular to the sound wave propagation direction (acoustic experiments) or current flow direction (electrical experiments), labeled "perpendicular orientation"; (b) aggregates cut with the (001) cleavage parallel to the measurements, labeled "parallel orientation"; and (c) aggregates with no preferred crystal alignment, synthesized by hot-pressing talc powder from the same starting material in a piston-cylinder apparatus, labeled "random orientation". Samples with a "random orientation" were synthesized by crushing the starting material into a powder and loading the powder into an Au capsule. The capsule was placed in a 0.5" Pyrex-talc cell, cold pressed to 1.5 GPa, and then annealed at 773 K for 12 hr. The retrieved samples are cylinders of ∼1.2 mm height and ∼1.5 mm diameter.

2.2. Ultrasonic Experiments

Ultrasonic experiments were conducted using a Paris-Edinburgh (PE) press at the High Pressure Collaborative Access Team (HPCAT) beamline (16-BM-B) of the Advanced Photon Source synchrotron, Argonne National Laboratory. Experimental conditions are listed in Table 2, and a schematic of the cell assembly is shown in Figure S1a in Supporting Information S1. The cylindrical talc samples with different orientations (Section 2.1) were placed in an MgO ring with an inner diameter of 1.5 mm and thickness of 1.2 mm. Two Au foils (each with a ∼2 μm thickness) were placed in direct contact with the two circular end faces of the cylindrical sample. Two Al_2O_3 rods with polished end surfaces were located on both sides of the sample and served as a buffer rod and backing plate. A hexagonal-BN spacer rod was located below the bottom buffer rod. All the MgO, Al_2O_3, and BN parts were inserted in a hexagonal-BN sleeve placed in a graphite heater. Pressure was calculated in situ by measuring the unit cell volume of the MgO capsule via energy-dispersive XRD and the equation of state from Kono et al. (2010). The experiments were conducted without a thermocouple, and temperature was estimated using a pre-calibrated power-temperature relationship, with typical temperature uncertainty of ∼10% (Kono et al., 2014).

A 10° Y-cut $LiNbO_3$ transducer was attached to the top WC anvil to generate and receive the compressional and shear wave signals from 16 to 48 MHz. The travel time, t, of the sample was determined using the buffer-rod/sample reflection, R_1, and sample/backing-rod reflection, R_2, identified using the SonicPy software suite (Hrubiak & Sturtevant, 2023). The travel time was calculated through extrapolating the cross-correlation of the coupled reflections at multiple frequencies to infinite frequency. Sample thickness, l, was measured using in situ X-ray radiographs of the sample. Sound velocities, V, were calculated as follows:

$$V = 2l/t. \quad (1)$$

Table 2
Conditions for the Acoustic Experiments

Run #	Sample orientation	Pressure range (GPa)	Temp. range (K)
A1	Parallel	0.5–1.4	300–873
A2	Random	0.6–3.4	300–873
A3	Parallel	0.5–3.0	300–873
A4	Perpendicular	0.5–3.4	300–873

Table 3
Conditions for the Electrical Experiments and Fitted Arrhenius Equation Parameters for the Last Heating Cycle

					Arrhenius parameters, segment 1			Arrhenius parameters, segment 2		
Run #	Sample orientation	Pressure (GPa)	Quenching Temp. (K)	Sample thickness (mm)	T range (K)	Ln σ_0 (σ_0 in S/m)	ΔH (kJ/mol)	T range (K)	Ln σ_0 (σ_0 in S/m)	ΔH (kJ/mol)
BBC46	Perpendicular	1.5	1263	1.22 (8)[a]	–	–	–	1026–1064	11.5 (1.7)	158.5 (14.4)
BBC47	Parallel	1.5	1223	1.20 (5)	–	–	–	1012–1067	26.1 (1.8)	296.2 (15.8)
BBC53	Parallel	1.5	1038	1.23 (10)	816–1012	0.0 (0.4)	90.0 (2.9)	–	–	–
BBC55	Parallel	2.5	1213	1.18 (5)	825–985	−0.3 (0.2)	52.3 (1.4)	1007–1054	23.1 (1.6)	245.9 (14.1)
BBC48	Perpendicular	3.5	1173	1.18 (10)	881–933	4.6 (0.7)	98.7 (5.3)	973–999	18.0 (3.4)	193.6 (28.0)
BBC49	Parallel	3.5	1198	1.23 (9)	837–968	3.2 (0.3)	81.8 (1.9)	968–1013	12.0 (1.9)	145.8 (13.9)
BBC56	Parallel	6.0	1043	1.10 (5)	690–846	5.5 (0.1)	90.1 (0.6)	866–938	10.9 (0.7)	118.7 (5.4)

[a]All numbers in parentheses are standard deviations.

Velocity errors, ΔV, are estimated by fitting the travel time and sample thickness errors, Δt and Δl, respectively:

$$\Delta V = V\sqrt{\left(\frac{\Delta l}{l}\right)^2 + \left(\frac{\Delta t}{t}\right)^2}. \quad (2)$$

ΔV is typically <1.3%.

2.3. Electrical Experiments

Electrical experiments were carried out at the Earth and Planets Laboratory (Carnegie Institution for Science) using a 1,100-ton Walker-type multi-anvil apparatus and 14/8 (COMPRES) cell assemblies with WC cubes (e.g., Pommier et al., 2019). Experimental conditions are listed in Table 3, and a schematic of the cell assembly is shown in Figure S1B in Supporting Information S1. The cylindrical sample was placed in an alumina sleeve with an inner diameter of 1.5 mm and thickness of 1.2 mm. Two iron disks (~2.5 mm diameter) were placed in direct contact with the sample to serve as electrodes, while two alumina rings were placed on each side of the sample sleeve to aid fluid retention. The sample was heated by applying a current to a surrounding rhenium foil, with temperature measured using two Type-C ($W_{95}Re_5$-$W_{74}Re_{26}$) thermocouples that also served as electrodes. All MgO components were dehydrated at >1273 K and then stored in a desiccator until use.

Talc conductivity was measured up to 1263 K at four different pressures: 1.5, 2.5, 3.5, and 6 GPa (Table 3). For most experiments, complex impedance spectra were collected during heating and cooling cycles to assess reproducibility. A DC potential of 1 V with an AC amplitude of 1,000 mV was applied over a frequency range of 1 MHz to ~0.1 Hz. Pressure was first increased to the target value, and temperature then increased to 773 K. A pre-heating step lasting 1.5 hr was performed at <773 K—well below the breakdown temperature of talc (Berman, 1988; Bose & Ganguly, 1995; Pawley & Wood, 1995)—to remove possible moisture from the assembly (Figure S2 in Supporting Information S1). Impedance measurements were performed every ~25 K. When a change in resistance was observed, impedance spectra were collected at a fixed temperature until a stable electrical response was reached. At the end of the experiment, the sample was quenched by cutting power to the heater.

Electrical measurements were performed using a Solartron 1260 A gain/phase analyzer. The complex impedance (Z^*) of the sample, the middle alumina sleeve, and the two electrode disks was measured over the frequency range and consists of a real part (Z') and an imaginary part (Z'') (Huebner & Dillenburg, 1995). In a Nyquist plot (Z'' vs. Z'), the bulk electrical resistance is determined from the intersection or extrapolated intersection of the impedance arc and the horizontal axis (Z'). The calculated bulk resistance of the sample (R) was corrected for minor contributions from the Al_2O_3 ring and two Fe electrode disks. Conductivity (σ) was then calculated using:

$$\sigma = l/(A \times R) \quad (3)$$

where A is the surface area of the sample, and l is the sample thickness determined from a backscattered electron (BSE) image of the retrieved sample. The fractional uncertainty of the conductivity was calculated using:

$$\left|\frac{\Delta\sigma}{\sigma}\right| = \sqrt{\left(\frac{\Delta l}{l}\right)^2 + 4\left(\frac{\Delta r}{r}\right)^2 + \left(\frac{\Delta R}{R}\right)^2} \quad (4)$$

where $\Delta\sigma$, Δl, Δr, and ΔR represent the error of electrical conductivity, sample thickness, sample radius, and electrical resistance, respectively. Conductivity errors are typically <10% (Hao et al., 2024; Saxena et al., 2021).

2.4. Analytical Techniques

All retrieved samples were mounted in epoxy and polished for textural and chemical analyses using a JEOL 8530F electron microprobe. An accelerating voltage of 15 kV and beam current of 30 nA were used. Wavelength dispersive spectroscopy was performed with integration times of 30 s on peak and 15 s on background. The following standards were used: hornblende for Mg, Ca, and Fe; albite for Na; orthoclase for K, Al, and Si; ilmenite for Mn and Ti; and magnesiochromite for Cr. In addition, X-ray diffraction (XRD) and Raman spectroscopy analyses were performed on the starting material, the material sintered at 1.5 GPa and 773K, and the sample retrieved from electrical experiment BBC53 to determine the material structure. XRD analyses were conducted using a Bruker D8 Discover instrument with a Cu microfocus source from 10° to 50° 2θ and a total exposure time of 300 s. Raman spectra were collected using a Witec α-SNOM (scanning near-field optical microscope) equipped with a confocal Raman spectroscopic imaging capability. The excitation wavelength was 532 nm, and the power at the sample was 0.3–1 mW. We collected a series of Raman spectroscopic images (50 × 50 μm imaged areas), which were then averaged across areas of interest to produce Raman spectra from each phase. The spatial resolution was 1 μm. The Raman spectra were collected through a Peltier-cooled Andor EMCCD system. The scattered light was dispersed with a 600-groove/mm grating, and Raman spectra in the spectral bandwidth of 0–3,700 cm^{-1} were collected with an integration time of 1 s/pixel. Processing of raw spectra was performed using the WITec software (Project Plus version 5.3) to remove any signals from cosmic rays and to subtract a broad emission background. In addition, principal component analysis (PCA) was performed on the Raman spectra collected within selected imaged areas.

To estimate the effect of crystal orientation on acoustic velocity measurements, one ultrasonic experiment sample (A1, parallel orientation; Table 2) was prepared for electron backscatter diffraction (EBSD) analysis. The sample was cut along the main compression direction of the PE press, polished using diamond suspension down to 0.5 μm, and vibratory polished for 1 hr in colloidal silica solution (Buehler MasterMet). EBSD data were collected at the Marine Biological Laboratory (Woods Hole, MA) using an Oxford Instruments Symmetry detector attached to a Zeiss Supra 40VP FEG-SEM. EBSD map data were collected at a step size of 5 μm under low-vacuum conditions, with an accelerating voltage of 20 kV, working distance of 19 mm, and 70° stage tilt. To account for the weak EBSD patterns produced by talc, 100 patterns were averaged at each beam spot with a dwell time of 5 milliseconds for each pattern. To further improve the signal-to-noise ratio, the EBSD detector was reduced to a resolution of 622 × 512 pixels (i.e., 2 × 2 binning). EBSD patterns were indexed using two methods: (a) a typical automated method based on the Hough transform, and (b) a pattern matching approach using Oxford Instruments' MapSweeper post-processing package. Hough-based indexing was conducted by fitting up to 11 bands at a Hough resolution of 60, using unit cell parameters for triclinic talc ($a = 5.2957$ Å; $b = 9.1810$ Å; $c = 9.4228$ Å; $\alpha = 90.4°$; $\beta = 98.9°$; $\gamma = 90.1°$). Indexed solutions with mean angular deviation values greater than 1° were discarded, giving a final hit rate of 9.7%. MapSweeper analyses were performed by comparing each experimental pattern to a reference pattern generated via kinematic simulation (using the same unit cell parameters as above). The whole data set was first reprocessed using dynamic template matching at 38 × 32 pixel resolution and 2° orientation spacing. The best-fit solutions were then further refined at 77 × 64 pixel resolution. Finally, solutions with normalized cross-correlation coefficients <0.2 were discarded, giving a final hit-rate of 78%. Examples are provided in Figure S3 in Supporting Information S1. Similar orientation results are obtained regardless of which indexing method was used (Figure S4 in Supporting Information S1), but we herein use the MapSweeper results to ensure statistical significance. Further EBSD data post-processing was performed in the MTEX toolbox for MATLAB (Bachmann et al., 2010).

Table 4
Electron Microprobe Analyses of the Starting Material and Retrieved Samples (in wt.%)

Sample	Phase	SiO_2	TiO_2	Al_2O_3	Cr_2O_3	FeO	MnO	MgO	CaO	Na_2O	K_2O	Total
Starting material	Talc (8)[a]	62.9 (5)[b]	0.01 (0)	0.07 (1)	0.01 (1)	0.50 (1)	0.00 (0)	32.2 (3)	0.23 (8)	0.07 (3)	0.01 (0)	95.9
BBC46	En (9)	59.4 (3)	–	0.44 (11)	–	0.68 (4)	–	40.2 (2)	0.03 (2)	–	–	100.8
	Qz (1)	100.9	–	0.03	–	0.04	–	0.16	0.01	–	–	101.1
BBC47	En (11)	59.2 (2)	–	0.46 (24)	–	0.66 (3)	–	40.2 (2)	0.02 (1)	–	–	100.6
BBC48	En (5)	59.4 (1)	–	0.31 (13)	–	0.73 (5)	–	40.1 (2)	0.04 (3)	–	–	100.5
BBC49	En (6)	59.3 (1)	–	0.42 (11)	–	0.69 (3)	–	40.1 (1)	0.05 (2)	–	–	100.5
	Qz (1)	99.3	–	0.11	–	0.06	–	2.04	0.01	–	–	101.5
	Talc (1)	63.2	–	0.74	–	0.59	–	32.1	0.03	–	–	96.7
BBC53	Talc (17)	63.5 (2)	–	0.07 (1)	–	0.53 (2)	–	31.4 (2)	0.00 (0)	–	–	95.4
BBC55	En (12)	59.2 (2)	–	0.57 (17)	–	0.65 (5)	–	40.0 (2)	0.01 (1)	–	–	100.4
	Qz (2)	101.2 (4)	–	0.04 (1)	–	0.05 (1)	–	0.27 (0)	0.00 (0)	–	–	101.6

Note. En = enstatite, Qz = quartz (or coesite). [a]Number of analyses. [b]One standard deviation in terms of last unit cited.

3. Results

3.1. Composition and Texture of Retrieved Samples

Representative backscattered electron (BSE) images and energy dispersive spectroscopy (EDS) maps of the starting material and retrieved samples are shown in Figure 1. Talc is the only phase in the starting material, and the anisotropic structure of talc grains is visible (Figure 1a). The samples retrieved from the acoustic experiments remained exclusively composed of talc. All acoustic samples have talc (001) planes aligned perpendicular to the velocity measurement direction (Figure 1b), despite their different initial orientations. The retrieved electrical samples are composed of talc breakdown products, enstatite and quartz (Figures 1c and 1d), with the exception of sample BBC53, which was quenched at the lowest temperature (1038 K; Table 3) and contains only talc. A few isolated talc grains are also observed in sample BBC49. Enstatite grains are 10–30 μm in diameter and are generally larger than SiO_2 grains (5–10 μm).

At the sample scale, the phases are well distributed for all electrical experiment samples quenched at low temperatures (≤1150 K). For electrical samples quenched at high temperature, porosity is lower at the center of the sample than in the outer portion. The outer portion is characterized by an abundance of circular pores (Figures 1c and 1d), contrasting with a compacted, low-porosity texture of the inner portion (Figure 1e). This textural variation is reflected in Si maps (Figure 1f) and probably indicates the presence (and then escape) of a free fluid phase following talc breakdown.

Quantitative chemical analyses of the retrieved electrical samples are listed in Table 4. The low totals (95.4–96.7 wt.%) obtained for talc are consistent with the presence of structural water. Enstatite and the silica phase have a consistent composition across all experiments. Most enstatite crystals reveal a composition close to $MgSiO_3$, with small amounts of iron (~0.7 wt.% FeO) and Al_2O_3 (0.57 wt.% or less). Based on a combination of microscopic observations and microprobe traverses (Figure S5 in Supporting Information S1), sample contamination during the electrical experiments can be summarized as follows. First, at the alumina sleeve-sample interface, a very thin (<~40 μm) Al-rich layer is observed in the sample. This layer is expected to have a negligible effect on conductivity (Pommier et al., 2019). Second, contamination of the sample by the Fe disks occurs over a range <40 μm from the electrode. In this part of the sample, a depletion in Mg (and, to a lesser extent, in Si) is observed. The electrical results are not significantly affected (error <10%) by Fe contamination (Pommier & Leinenweber, 2018). No contamination from the cell parts is observed in the acoustic samples, which can be attributed to the low-temperature conditions of these experiments.

Talc orientations are presented as EBSD contoured pole figures in Figure 2a for acoustic sample A1. There is a strong crystallographic preferred orientation (CPO) with (001) cleavage planes oriented perpendicular to the ultrasonic wave propagation direction—consistent with BSE observations (Figure 2b)—despite the initial parallel orientation. The [100] and [010] crystal axes show either broad point maxima (Figure 2a) or weak girdles

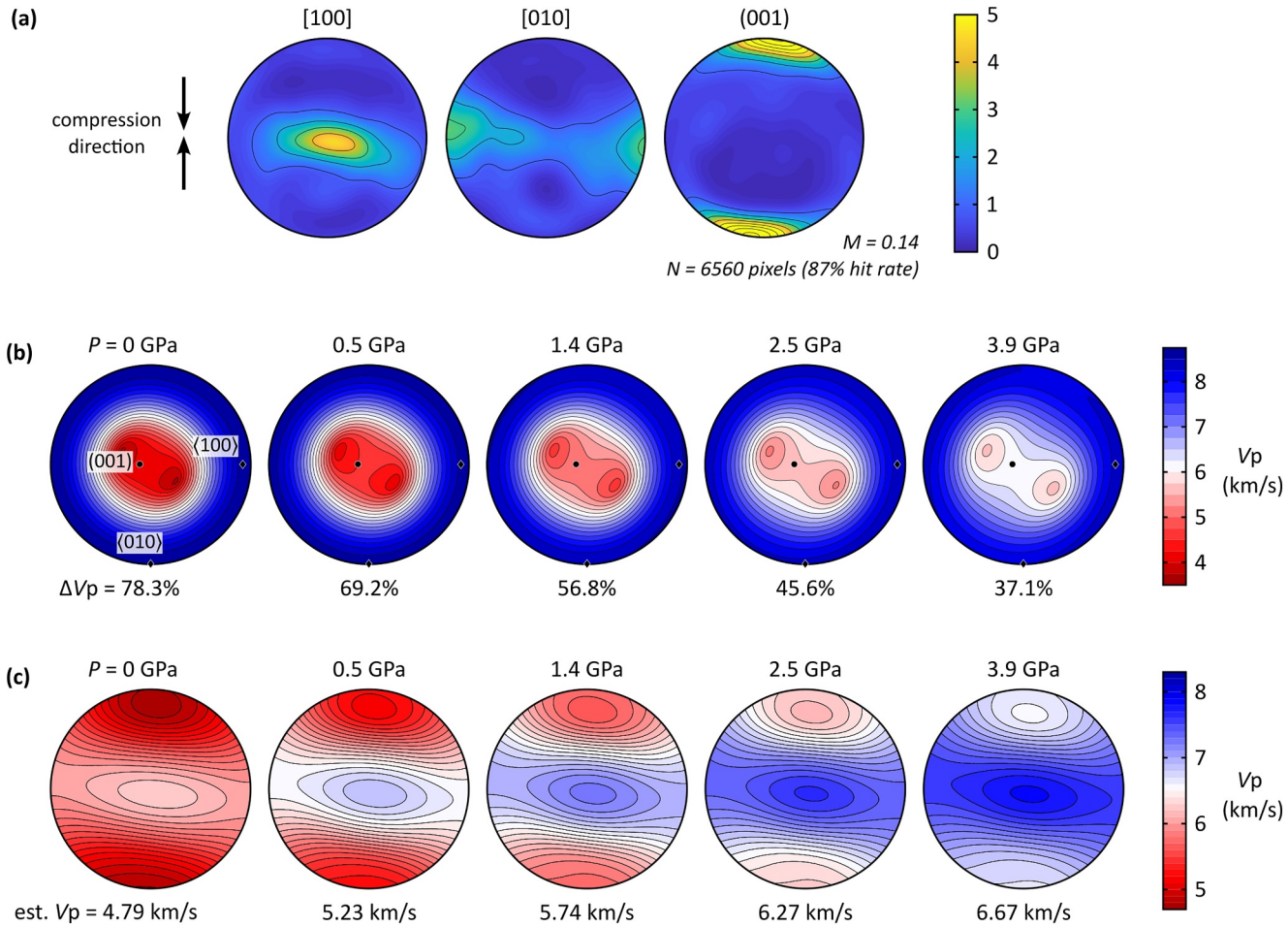

Figure 2. Pole figures showing the crystal-preferred orientation (CPO) and P-wave velocities (*Vp*) of the talc sample retrieved from ultrasonic experiment A1. (a) Lower-hemisphere, equal-area pole figures showing the orientations of the talc [100], [010], and (001) directions, calculated from the map re-indexed using the MapSweeper pattern matching technique. Pole figures are contoured using a half width of 10° using the all-pixels orientation data. The color bar represents the intensity of the CPO in multiples of uniform distribution. (b) P-wave (*Vp*) velocities of a talc single crystal, as a function of pressure *P*, calculated using the elastic constants from Peng et al. (2022). *Vp* anisotropy (Δ*Vp*) is given as a percentage at each pressure. (c) *Vp* pole figures estimated as a function of pressure using the orientation data for sample A1 and elastic constants from Peng et al. (2022), with Voigt-Reuss-Hill averaging. At each pressure, the estimated *Vp* value parallel to the measurement and compression direction is shown (vertical in all pole figures).

(Figure S4a in Supporting Information S1) within the plane normal to compression, depending on the indexing method. This CPO is consistent with previous EBSD measurements for naturally deformed talc samples (Lee et al., 2020; Nagaya et al., 2020).

XRD and Raman spectroscopy results are shown in Figure S8 in Supporting Information S1. The XRD spectra of the starting material and sintered material at 773 K and 1.5 GPa are identical. However, the presence of a new XRD peak is visible at a 2θ value of ∼44° for sample BBC53, quenched at 1038 K and 1.5 GPa. The Raman spectra of the starting material and sample BBC53 are similar and indicate that talc is the only phase present.

3.2. Sound Velocities

Examples of ultrasonic spectra for different talc samples at selected pressure-temperature conditions are shown in Figure S6 in Supporting Information S1. The reflections of compressional waves are clearly identified at 0.5–3.5 GPa and 300–873 K, allowing the calculation of compressional wave velocities (*Vp*). In contrast, reflection R_2 of the shear wave overlaps with the double reflections of R_0 ($2R_0$), making the calculation of shear wave velocities (*Vs*) challenging. Consequently, only *Vp* values of talc are reported in this study.

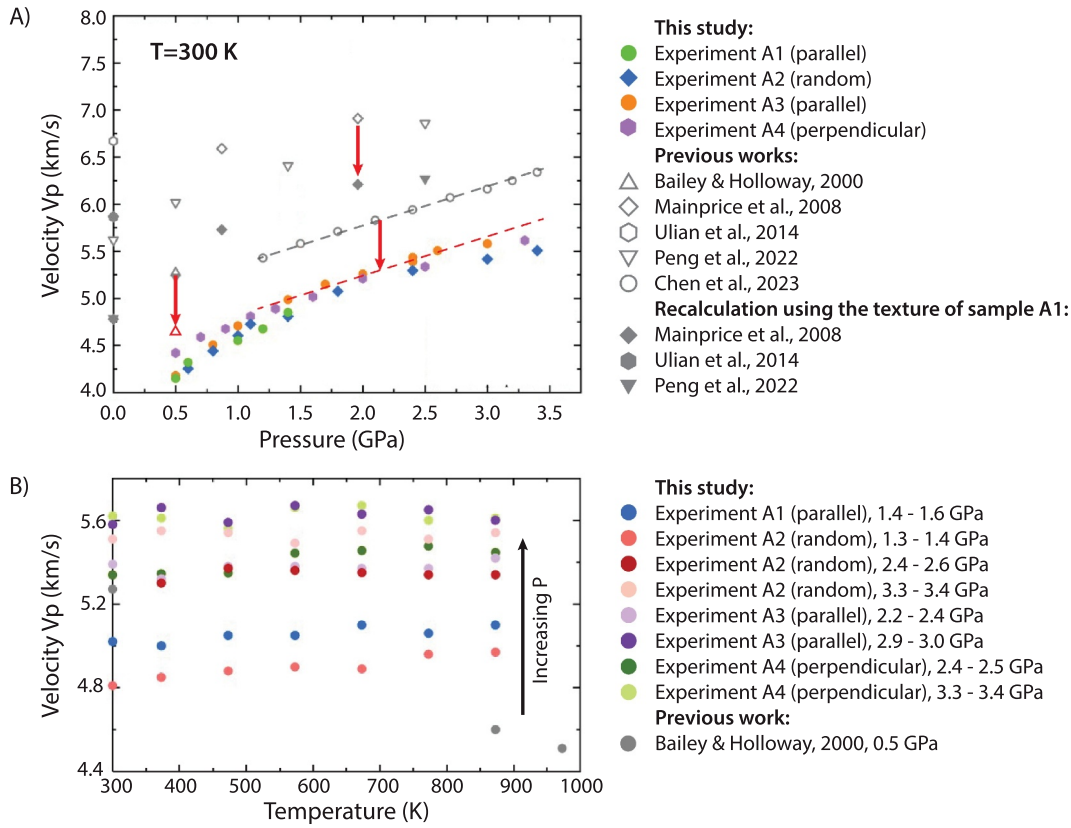

Figure 3. *Vp* velocity values of the talc samples (in color) and comparison with previous studies (in gray). (a) *Vp* values at room temperature (300 K) and different pressures. Colors indicate different initial crystallographic orientations of the starting material (perpendicular, parallel, or random orientation) and show negligible elastic anisotropy. Filled gray symbols correspond to recalculated *Vp* values from previous theoretical works on talc aggregates with randomly oriented grains (Mainprice et al., 2008; Peng et al., 2022; Ulian et al., 2014) using the texture of sample A1 (see Text S1 in Supporting Information S1). These recalculated velocities are lower than values retrieved from first-principles studies (open gray symbols, see Text S1 in Supporting Information S1), as illustrated by the top vertical red arrow. The red dashed line and red open triangle associated with the other two vertical arrows show the effect of a correction of ~0.6 km/s on the experimental results of Chen et al. (2023) and Bailey and Holloway (2000), respectively. See text for details. (b) *Vp* values as a function of temperature. Colors indicate different pressure ranges and crystallographic orientations of the starting material. The estimated error on each data point is smaller than the marker size.

The *Vp* values for all samples are presented in Figure 3. *Vp* increases nonlinearly with pressure from ~4.25 km/s at 0.5 GPa to ~5.5 km/s at 3.4 GPa. No effect of sample orientation (parallel, perpendicular, and random orientations) is observed; at any given pressure, variation in *Vp* values among the three samples is ≤0.3 km/s. The pressure dependence is reproduced using the following polynomial equation:

$$Vp = -0.14 \times P^2 + 0.99 \times P + 3.80 \quad (5)$$

where pressure, *P*, is in GPa, and *Vp* is in km/s ($R^2 = 0.96$). Temperature has a negligible effect on *Vp* (Figure 3b), with values varying by <0.2 km/s between 300 and 873 K.

3.3. Electrical Conductivity

Typical impedance spectra collected at different temperatures and pressures are presented in Figure S7 in Supporting Information S1. Most impedance spectra consist of a single arc, with its size decreasing with increasing temperature. A second arc is sometimes observed and overlaps with the first arc. Because talc is the only phase observed in the starting materials, the second arc is likely due to grain boundary effects (e.g., Yoshino, 2010). In some cases, only a portion of the arc is observed at high temperature, because of noise at high frequency.

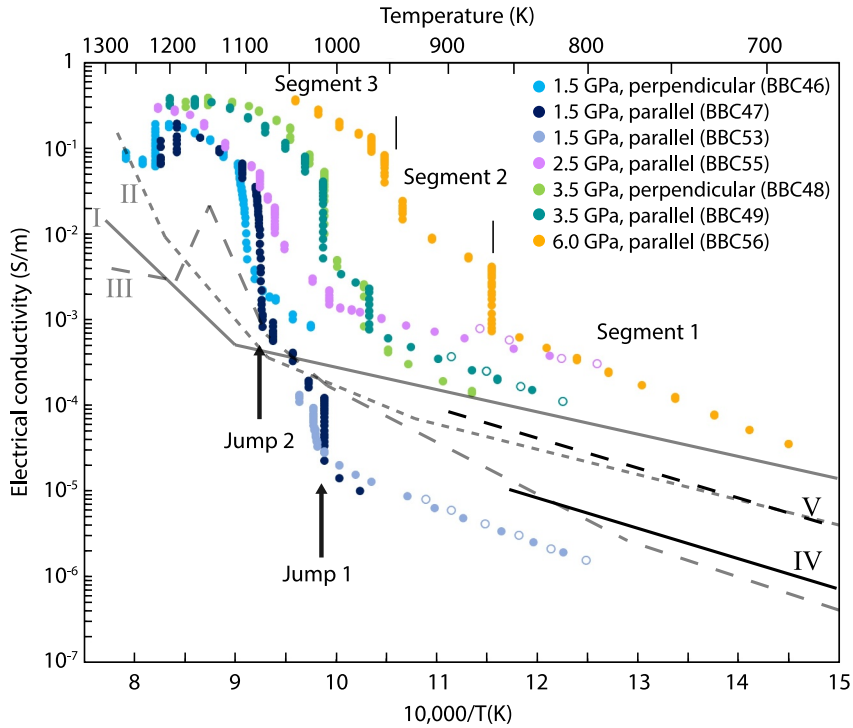

Figure 4. Electrical conductivity of talc as a function of inverse temperature for different pressures and sample loading orientations. Filled circles indicate data collected during heating, and open circles data collected during cooling. At fixed pressure, each conductivity trend can be divided into three segments (indicated for experiment BBC56). Conductivity jumps are observed in all experiments (indicated with vertical black arrows for experiment BBC47). Comparison with previous electrical studies of talc is also shown. I: Wang et al., 2020 (1.0 GPa); II: Wang et al., 2020 (3.5 GPa); III: Wang & Karato, 2013 (0.5 GPa); IV: Guo et al., 2011 (3 GPa, perpendicular); V: Guo et al., 2011 (3 GPa, parallel).

Examples of the equivalent electric circuits are shown in Figure S7 in Supporting Information S1 and values of the circuit components are listed in Table S1 in Supporting Information S1.

Temperature-dependent conductivity values are shown in Figure 4. For all experiments except BBC46, 48, and 56 (one heating cycle), electrical conductivity is similar during cooling and subsequent heating cycles. At each pressure, the electrical conductivity of talc increases nonlinearly with increasing temperature, and two conductivity jumps separate the entire temperature range into three segments. In the two low-temperature segments (<953–1083 K, depending on pressure), conductivity increases linearly with temperature. In the high-temperature segment (>953–1083 K), conductivity increases with temperature to attain a plateau at ~1100–1150 K. The first conductivity jump is observed at 873–1010 K and corresponds to an increase in conductivity by a factor of up to 10 for all experiments. The second jump occurs at 953–1083 K, with an increase in conductivity by a factor of ~10–100. Experiments BBC47 and BBC53 (1.5 GPa and parallel sample orientation) show reproducibility in the temperature of the first jump.

An Arrhenius equation is used to reproduce electrical conductivity in segments 1 and 2:

$$\sigma = \sigma_0 \times \exp\left(\frac{-\Delta H}{RT}\right) \tag{6}$$

where σ_0 is the preexponential factor, ΔH is the activation enthalpy, R is the gas constant, and T is the temperature. Values of these parameters are provided in Table 3. The activation enthalpy of the dominant conduction mechanism ranges from 52 to 99 kJ/mol for segment 1 and 119–296 kJ/mol for segment 2. No clear dependence of ΔH to pressure or sample loading orientation is observed.

Additionally, no systematic effect of pressure on conductivity is observed, though the experiment performed at the highest pressure (6 GPa; BBC56) is the most conductive. Within segment 1, conductivity varies by at least two

log units at a given temperature, depending on pressure. The magnitude of these conductivity changes decreases as temperature increases. For example, at high temperature (segment 3), the conductivity at each pressure tends to converge to a value of ~0.2–0.5 S/m (Figure 4). This electrical plateau is disrupted in two experiments (BBC46 and BBC47) that show a sharp decrease in conductivity at ~1200 K. We attribute this increase in resistance to the loss of fluids from the electrical cell, as previously observed for lawsonite aggregates (Pommier et al., 2019).

4. Discussion

4.1. Acoustic Properties of Talc

The *Vp* values of our talc samples are >0.8 km/s lower than those previously reported over a similar range of pressure and temperature conditions (Figure 3). Further details about the use of previous first-principles studies (as shown in Figure 3) are provided in Text S1 in Supporting Information S1. At room temperature and 0.5–3.4 GPa, our samples have a *Vp* velocity in the range ~4.1–5.7 km/s. In comparison, *Vp* values from previous studies at comparable pressure range from ~5.25 to 6.9 km/s, based on acoustic measurements (5.25–6.3 km/s; Bailey & Holloway, 2000; Chen et al., 2023) and first principles calculations for $Mg_3Si_4O_{10}(OH)_2$ (6.0–6.9 km/s; Mainprice et al., 2008; Ulian et al., 2014; Peng et al., 2022). The strong anisotropy of talc (e.g., Peng et al., 2022) can explain the range of values in previously determined elastic properties, with the lowest *Vp* values being in the direction perpendicular to the (001) plane. However, no significant elastic anisotropy is observed in our measurements, with *Vp* values varying by less than 0.3 km/s among all samples (Figure 3a), despite the initial sample orientation in the press (perpendicular, parallel, or random; Table 2). We ascribe the lack of elastic anisotropy in our measurements to the reorientation of talc grains under uniaxial stress during compression in the Paris-Edinburgh press. The extreme mechanical weakness of talc likely facilitates this textural change. Grain reorientation is supported by the EBSD analyses of sample A1 (Figure 2)—this sample was initially loaded in the Paris-Edinburgh press with (001) planes parallel to the compression direction but shows realignment of (001) cleavage planes perpendicular to the compression direction after the experiment. The limited variation in *Vp* values from our experiments for the different sample orientations at the lowest pressure (0.5 GPa) and at room temperature suggests that talc realignment occurs early in the compression, before heating the sample.

The effect of talc texture on the discrepancy between our *Vp* values and previous data from the literature can be investigated further by recalculating *Vp* velocity values from previous works on randomly orientated aggregates for a talc texture similar to that of sample A1 (Figure 2). These calculations considered talc elastic constants from the first-principles studies, that is, Mainprice et al. (2008), Ulian et al. (2014), and Peng et al. (2022) (Text S1 in Supporting Information S1). We observe that the *Vp* values calculated for talc with a CPO mimicking that observed in sample A1 are 0.5–1 km/s lower than the original values from first-principles studies (Figure 3a). The recalculated values are in better agreement with our velocities but remain slightly higher than our *Vp* values. Variations in talc chemistry (e.g., the presence of impurities found in our natural talc samples but not considered in first-principles calculations) possibly explains the remaining discrepancy. If we apply a similar correction for texture (~0.6 km/s) to the previous experimental results of Bailey and Holloway (2000) and Chen et al. (2023), a significantly improved agreement with our experimental data is obtained (Figure 3a). These calculations suggest that sample texture (i.e., CPO) best explains the difference in *Vp* values observed between our measurements and velocity data from previous first-principles and experimental studies.

4.2. Electrical Properties of Talc

Activation enthalpy values in segment 1 vary from 52 to 99 kJ/mol (Table 3), with no clear dependence on pressure or orientation. Overall, these values tend to be slightly higher than ΔH values for talc obtained at similar temperatures and consistent with a conduction mechanism dominated by protons (48–65 kJ/mol at T≤1023 K (Wang et al., 2020); 57–72 kJ/mol at T≤900 K (Guo et al., 2011)). Wang and Karato (2013) reported a ΔH value of 49 kJ/mol at T≤823 K and 131 kJ/mol at 823–1078 K, but suggested that small polaron conduction—that is, electron hopping between Fe^{2+} and Fe^{3+}—dominates over the entire T range (473–1078 K). Our ΔH values for segment 1 are compatible with a conduction mechanism dominated by contributions from both protons and small polarons.

The activation enthalpy in segment 2 (119–296 kJ/mol), which is delimited by the two jumps in conductivity, is substantially higher than in segment 1 for all experiments (Table 3). These values are too high to be compatible with a significant contribution from protons and, rather, indicate a dominant contribution from small polarons and

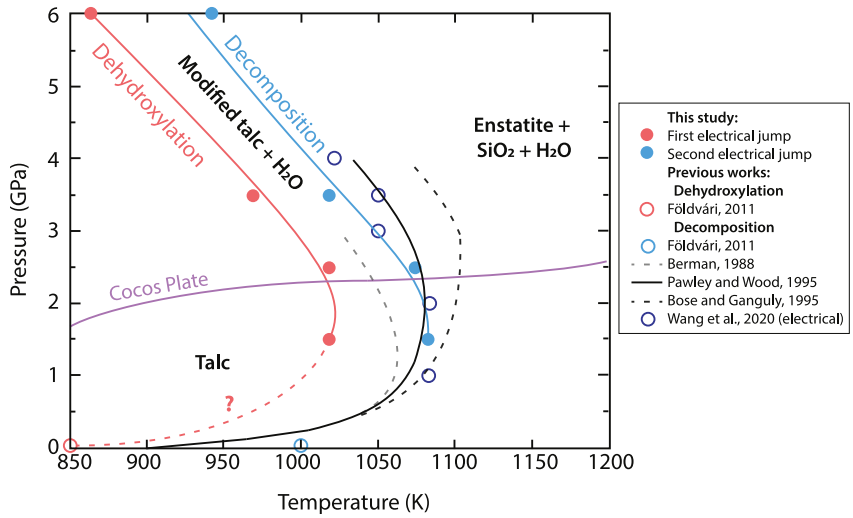

Figure 5. Comparison of the two jumps in electrical conductivity with the stability of talc determined from previous phase equilibria and thermogravimetric studies (dashed and full black/gray lines; Berman, 1988; Pawley & Wood, 1995; Bose & Ganguly, 1995; Földvári, 2011). The first jump is compatible with dehydroxylation (red circles and line), and the second jump is consistent with talc decomposition into enstatite, SiO_2 and water (blue circles and line). Conductivity values from Wang et al. (2020) interpreted as the onset of dehydration (decomposition) are also indicated with dark blue open circles. The surface temperature of Cocos plate (Syracuse et al., 2010) is shown for comparison. See text for details.

cation (Mg) vacancies. The contribution from cations is in agreement with diffusion studies of hydrous silicates minerals at similar temperatures, which reported activation enthalpy values for cation diffusion typically >140 kJ/mol (e.g., Fortier & Giletti, 1991; Brady, 1995 and references therein).

Electron microprobe analyses show that the sample quenched immediately after the first jump (BBC53) has a composition similar to that of the starting material (Table 4). Raman spectroscopy analyses performed on the starting material and sample BBC53 also indicate that no new phase was formed during the first jump (Figure S8 in Supporting Information S1). In addition, comparison of the temperature of this jump with phase equilibrium studies (Berman, 1988; Pawley & Wood, 1995; Bose & Ganguly, 1995; Figure 5) highlights that the sharp increase in conductivity is not consistent with the breakdown of talc into enstatite, SiO_2, and H_2O. However, our XRD analyses show a new peak for sample BBC53 quenched after the first conductivity jump (Figure S8 in Supporting Information S1), which is consistent with a structural transformation of talc. Talc dehydroxylation is expected at low temperature, that is, below the decomposition temperature, and this reaction results in a modified talc structure and the release of some water (e.g., Földvári, 2011 and references therein; Figure 5). Talc dehydroxylation has been characterized at atmospheric pressure using thermogravimetric measurements, which revealed a mass loss at a temperature below the decomposition into enstatite, SiO_2, and water (Figure S9 in Supporting Information S1; Földvári, 2011; Yi et al., 2019 and references therein). We propose that dehydroxylation is responsible for the first conductivity jump in our samples. The release of interlayer water during this reaction is possibly too minor to be detected using electron microprobe analyses and Raman spectroscopy, but the associated structural changes significantly affect bulk conductivity (Figure 4). It is likely that this reaction results in the formation of new defects in talc, which could explain the high activation enthalpy values in segment 2 (Table 3). The release of interlayer water associated with this low-temperature transformation could also increase grain boundary conduction. However, further work is required to fully understand the effect of dehydroxylation on conductivity. We note that the conductivity data from Wang and Karato (2013) can also be reproduced satisfactorily with an increase in ΔH from 131 to ~188 kJ/mol at ~1023 K (their Figure 3). This possible transition at 1023 K is consistent with the first jump observed in our experiments (848–1013 K). Different heating rates possibly explain why a change in slope, rather than a jump, was observed by Wang and Karato (2013), and why there was no change in conductivity observed by Guo et al. (2011), Wang et al. (2020), and Zhu et al. (2001).

The second conductivity jump is attributed to talc decomposition into enstatite, SiO_2 and H_2O. As shown in Figure 5, the pressure dependence of the decomposition temperature is comparable to that of the dehydroxylation temperature (first jump). Upon talc decomposition, conductivity increases by a factor of up to 100. An increase in

conductivity with a lower magnitude (factor of ∼10 or less) was observed by Wang and Karato (2013). Wang et al. (2020) also reported a significant increase in conductivity during and after talc breakdown. However, the data from Wang et al. (2020) do not indicate a conductivity jump, possibly because temperature was increased regularly during talc breakdown, which prevents discriminating between the separate effects of temperature and dehydration on conductivity.

After decomposition (segment 3), conductivity increases linearly over a limited T range (∼50 K) with an activation enthalpy similar to that of segment 2, before the attainment of a plateau value (Figure 4). Similar ΔH values suggest that the same conduction mechanisms as in segment 2 operate after talc decomposition. The limited influence of proton conduction on ΔH following talc dehydration has been previously invoked by Wang and Karato (2013), who also suggested that the small increase in conductivity after decomposition could be related to a change in oxygen fugacity (fO_2). The weak or negative temperature dependence of conductivity at the highest temperatures is consistent with the presence of a free fluid phase that gradually escapes from the cell. Small amounts (<200 ppm; Mierdel & Keppler, 2004) of structural water may also dissolve into the residual silicate matrix, yet the effect of small amounts of dissolved water in NAMs on bulk conductivity is negligible compared to that of a free fluid phase (e.g., Sinmyo & Keppler, 2017; Zhang et al., 2012).

BSE images of the samples quenched after the second jump show numerous circular pores (Figure 1), suggesting an interconnected aqueous fluid phase at the time of quenching. The conductivity of the fluid phase can be estimated using the Hashin-Shtrikman upper bound (Glover, 2015; Hashin & Shtrikman, 1962):

$$\sigma_{bulk} = \sigma_f \times \left[1 - \frac{3(1-\phi)(\sigma_f - \sigma_s)}{3\sigma_f - \phi(\sigma_f - \sigma_s)}\right] \quad (7)$$

where σ_{bulk}, σ_f and σ_s are respectively the bulk (measured) conductivity, the fluid-phase conductivity, and the solid-matrix conductivity. Following the equilibrium reaction $Mg_3Si_4O_{10}(OH)_2 = 3\ MgSiO_3 + SiO_2 + H_2O$, the volume fraction of fluid ϕ can be estimated from the respective amounts of enstatite and quartz. Based on the molecular weight and density of each breakdown product and assuming a fluid phase composition close to pure H_2O, the expected fluid content is ∼14 vol.% (with 69 vol.% enstatite and 17 vol.% quartz). The solid matrix conductivity is estimated at 1000 K using the previous works by Zhang et al., 2012 ("dry" enstatite at 3 GPa) and Wang et al., 2010 (quartz at 1 GPa). Using the geometric mean (Glover, 2015), the bulk conductivity of the solid matrix (σ_s), composed of 80 vol.% enstatite and 20 vol.% quartz, is $\sim 2.6 \times 10^{-3}$ S/m. Taking σ_{bulk} as the highest conductivity value following the second jump (∼0.2 S/m at 1.5 GPa and ∼0.4 S/m at 3.5 GPa; Figure 4), Equation 7 provides an estimate for the conductivity of the fluid phase of ∼2.1 and 4.2 S/m at 1.5 and 3.5 GPa, respectively. These values agree with fluid conductivity estimates from electrical measurements during lawsonite dehydration (2.5–6 S/m; Pommier et al., 2019) and are consistent with an aqueous fluid phase that contains dissolved ions, rather than pure water. As an example, the conductivity of H_2O − NaCl fluids with a molarity of 0.1 M (mol NaCl/l) (e.g., Sinmyo & Keppler, 2017) is comparable to our σ_f estimates.

Electrical anisotropy can be estimated at 1.5 GPa (segment 2) and 3.5 GPa (segment 1) by comparing measurements on samples with parallel and perpendicular starting orientations (Figure 4). At 1.5 GPa, $\sigma_{max}/\sigma_{min}$ is up to 10 over 1020–1070 K, with the perpendicular direction being most conductive, and $\sigma_{max}/\sigma_{min} \leq \sim 2$ is at 3.5 GPa over 870–970 K, with the parallel direction being most conductive. At a comparable pressure (3 GPa), Guo et al. (2011) reported electrical anisotropy values for talc >2, with measurements along the lineation direction being most conductive by up to a factor of ∼8 in the T range ∼625–830 K. This difference in electrical anisotropy is possibly explained by the different crystallography of the talc material used in both studies (monoclinic in Guo et al. (2011) and triclinic in our study).

4.3. Geophysical Implications

Talc has been invoked to explain geophysical anomalies in central Mexico (e.g., Peng et al., 2022). In particular, seismic observations have revealed an ultra-slow layer (USL) atop the flat portion of the Cocos slab (Dougherty et al., 2012; Kim et al., 2010; Song et al., 2009). The slab initially dips at ∼15° to 40–50 km depth, followed by a subhorizontal segment that extends for ∼150 km. The Cocos plate is relatively young (∼10–23 Ma; Pardo & Suárez, 1995), with surface-temperature estimates of the flat segment increasing from ∼773 K near the trench to ∼973 K away from the trench (Syracuse et al., 2010; van Keken and Wilson, 2023b). Actual temperatures could

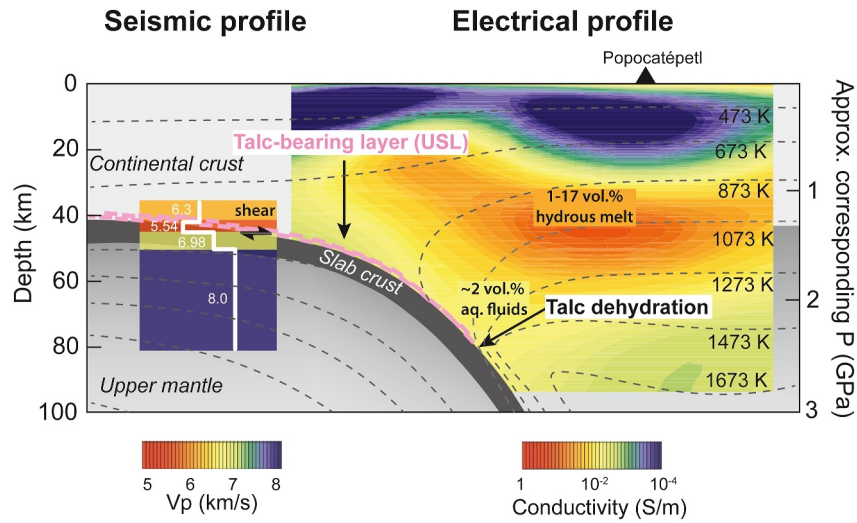

Figure 6. Schematic diagram of the talc-bearing subducted Cocos plate under central Mexico. The hypothetical talc-bearing layer at the top of the slab is indicated with pink dashes. The seismic (*Vp*) profile of the flat slab is from Kim et al. (2010). The electrical conductivity-depth map under central Mexico is modified after Jödicke et al. (2006). The horizontal color scale bars correspond to *Vp* velocity values (left) and electrical conductivity (right). The temperature profile is modified after Syracuse et al. (2010) and van Keken and Wilson (2023b). Our *Vp* measurements of talc with the (001) cleavage parallel to the slab surface reproduce field velocity values for a 3 km talc-bearing layer with <~30 vol.% talc and >~50 vol.% chlorite (see Text S2 and Figure S10a in Supporting Information S1). Talc dehydration is expected to occur at 70–80 km depth, from which fluids with a salinity equivalent to 0.1 M are released. Our electrical results are consistent with ~2 vol.% aqueous fluids at ~70 km depth. The conductive anomaly located at 20–50 km depth is compatible with ~1–17 vol.% hydrous melt containing 1 to 4 wt.% H_2O. See text for details.

be higher than the temperatures predicted by these steady-state models because of the amount of time needed for the overriding continent to cool (Liu et al., 2022). Talc is thought to originate from the mantle wedge during slab flattening (Kim et al., 2013), and petrological models support the production of talc along the Cocos plate interface via the advective transport of aqueous silica (Lindquist et al., 2023). The growth of a thick talc-bearing layer is a possible consequence of the migration and infiltration of silica-bearing fluids along the plate surface (Wilson et al., 2014). Talc is likely stable at this depth (corresponding pressure of ~1.5 GPa) because the mantle temperature (~1073 K) is lower than the dehydration temperature of talc (~1083 K). Talc is also expected to be stable at the interface between the slab and the overriding crust at this pressure (Peacock & Wang, 2021).

High conductivity anomalies are observed at ~70–80 km depth (~2.5 GPa) in a 75°-dipping segment beneath the flat slab (Figure 6; Jödicke et al., 2006), which is consistent with the dehydration of hydrous minerals, such as talc, chlorite, and/or amphibole (Mandler & Grove, 2016; Manthilake et al., 2016; Pawley & Wood, 1995). These minerals would increase bulk conductivity upon breakdown (Figures 4 and 5 for talc; Manthilake et al. (2016) for chlorite; Hu et al. (2018) for amphibole). However, the *Vp* values of chlorite (7.1–8.7 km/s; Mookherjee & Mainprice, 2014) and amphibole (6.6–7.6 km/s; Brown & Abramson, 2016) are significantly higher than those expected for the USL, considering a layer thickness of ~3 km derived from the best-fit model in previous seismic studies (*Vp* values of 5.4–6.2 km/s; Dougherty et al., 2012; Kim et al., 2010; Song et al., 2009). Thus, a talc-bearing layer is a viable candidate to explain both the seismic and electrical observations atop and near the subducted Cocos plate.

Flat subduction can induce a high degree of slab deformation, related especially to horizontal shear stresses at the surface (e.g., Behr & Smith, 2016). Being a very weak mineral, talc is expected to deform and develop a CPO similar to that observed in our acoustic experiments, with the (001) plane sub-parallel to the shear plane (i.e., slab surface). At the depth of the flat slab segment (~40–50 km depth), temperature estimates are in the range ~673–813 K (Syracuse et al., van Keken and Wilson, 2023b). Our measurements show that at these conditions, talc with an orientation perpendicular to (001) has a *Vp* of ~5.0 km/s (Figure 3), which is slower than field-based estimates (5.4–6.2 km/s; Song et al., 2009; Kim et al., 2010; Dougherty et al., 2012). We calculated the *Vp* velocity of a USL composed of talc + sediment + chlorite at 700 K using the iso-stress Reuss bound (Text S2 in Supporting

Information S1). As shown in Figure S10A in Supporting Information S1, field-based *Vp* estimates can be reproduced with various proportions of the three phases. However, realistic mineralogical assemblages can be defined based on previous petrological studies. First, chlorite is expected to be more abundant than talc in rocks undergoing Si-metasomatism (Codillo et al., 2022; Okamoto & Oyanagi, 2023). Second, up to 15 vol.% talc has been estimated in peridotite under water-saturated conditions (Hacker et al., 2003), but this estimate is a lower bound of the talc content at the slab-mantle interface because the high dissolved silica content in slab-derived fluids would favor extensive talc formation upon reaction with the overlying peridotite (Manning, 1995). These talc content estimates are consistent with field observations of exhumed high-pressure terranes thought to have originated along the slab mantle interface (e.g., Santa Catalina Island, USA; Arosa Zone, Switzerland) that indicate the presence of thin (cm- to m-scale) talc-rich layers at the interface of metamorphosed mafic and ultramafic lithologies (Bebout, 2013; Bebout & Barton, 2002; Condit et al., 2022). Our calculations show that a rock containing ∼12 vol.% talc and 70 vol.% chlorite or ∼23 vol.% talc and 50 vol.% chlorite reproduces the USL *Vp* velocity estimate of 5.54 km/s by Kim et al. (2010). Decreasing the amount of talc or decreasing the amount of chlorite will increase the *Vp* velocity of the USL (Figure S10A in Supporting Information S1). The corresponding bulk electrical conductivity of these assemblages can be estimated using the geometric mean and previous electrical studies of different minerals (Text S2 in Supporting Information S1). Given the range of talc conductivity values at low temperature (Figure 4), two values are considered. For a talc conductivity of 2×10^{-5} S/m (value at 1 GPa and 700 K from Wang et al., 2020), the conductivity of the USL is 9×10^{-6} S/m for a rock with 12 vol.% talc and 70 vol.% chlorite, and 8.5×10^{-6} S/m for a rock with 23 vol.% talc and 50 vol.% chlorite (Figure S10B in Supporting Information S1). For a talc conductivity of 3×10^{-7} S/m (extrapolation of data from BBC53 to 700 K), bulk conductivity decreases to 5.5×10^{-6} S/m if it contains ∼12 vol.% talc and 70 vol.% chlorite, and to 3.5×10^{-6} S/m if it contains ∼23 vol.% talc and 50 vol.% chlorite (Figure S10C in Supporting Information S1). Although both cases show different conductivity trends as the amount of talc varies (Figures S10b and S10c in Supporting Information S1), the conductivity values are always significantly lower than the conductivity of the surrounding mantle ($\sim 10^{-3}$ S/m; Jödicke et al., 2006), and the resistive USL might be too thin to be detected using electromagnetic observations.

At 70–80 km depth, conductivity is 0.02–0.03 S/m near the slab surface (Figure 6; Jödicke et al., 2006). These values are in agreement with the conductivity of the breakdown products of talc and an aqueous fluid content of ∼2 vol.% (using a fluid conductivity value of 2.1 S/m; see Section 4.2). Released fluids are expected to migrate upward and potentially induce partial melting at shallow depths (e.g., Sakuma & Ichiki, 2016; Schmidt & Poli, 2013). Partial melt could explain the field conductivity anomaly of 0.07–0.3 S/m located at 50–20 km depth (Figure 6; Jödicke et al., 2006). The amount of partial melt in the mantle wedge can also be estimated using Equation 7, assuming an olivine-hydrous basalt system. For this calculation, we considered the conductivity of hydrous basalt and "dry" olivine at 1473 K, using the previous results from Ni et al. (2011) extrapolated to the considered temperature and Gardés et al. (2014), respectively. The water content in the basaltic melt was varied from 1 to 4 wt.%, a range that is consistent with chemical analyses of melt inclusions from Popocatépetl (up to 3.4 wt.% H_2O; Atlas et al., 2006; Plank et al., 2013). The amount of hydrous basaltic melt needed to reproduce field values of 0.07 and 0.3 S/m is in the range 1.3–4 vol.% and 5.5–17 vol.%, respectively. These ranges are in general agreement with estimates from petrological studies (e.g., Grove et al., 2012).

5. Conclusions

We have investigated the acoustic and electrical properties of natural polycrystalline talc. Seismic velocity (*Vp*) measurements were performed up to 3.5 GPa and 873 K, and electrical measurements were conducted up to 6 GPa and 1223 K. Similar *Vp* values are obtained despite different initial crystallographic orientations of the samples, indicating a reorientation of talc grains during acoustic experiments in the uniaxial (Paris-Edinburgh) press. Electrical experiments reveal two distinct conductivity jumps, interpreted as dehydroxylation of the interlayer at low temperature (∼860–1025 K, depending on pressure) and as decomposition at high temperature (∼940–1080 K). Electrical anisotropy decreases with increasing pressure and is observed only at low temperature. At 1.5 GPa, the perpendicular orientation shows the highest conductivity, whereas at 3.5 GPa the parallel orientation is most conductive. Comparison of our acoustic and electrical conductivity results with geophysical observations of the Cocos Plate below central Mexico supports the presence of a talc-bearing layer at the top of the subducted plate, that undergoes dehydration at ∼70–80 km depth. A field *Vp* velocity value of 5.54 km/s for the USL is obtained for a 3-km thick layer made of talc, chlorite and sediment, with either 12 or 23 vol.% talc coexisting,

respectively, with 70 or 50 vol.% chlorite. The corresponding conductivity of the same rocks is low, with estimates ranging from 3.5×10^{-6} to 9×10^{-6} S/m. This study shows that the combination of acoustic and electrical experiments is a powerful approach to investigate the structure of subduction zones and the related volatile cycle.

Data Availability Statement

All the data can be found in Mendeley Data Repository (Hao et al., 2024).

Acknowledgments
The authors thank Victor Lugo for providing the starting material (natural talc), and Curtis Kenney-Benson for providing the cell assemblies for the acoustic experiments. We are grateful to Emma Bullock, Timothy Strobel, Andrew Steele, and Pat Trimby for their help with electron microprobe analyses, XRD, Raman spectroscopy, and MapSweeper analyses, respectively. We thank Peter van Keken for providing the thermal model used in Figure 6. AP thanks Michael J. Tauber for fruitful discussion, and acknowledges support from NSF-CAREER award EAR-1750746 and the Carnegie endowment. Acoustic experiments were performed at HPCAT (Sector 16), Advanced Photon Source (APS), Argonne National Laboratory. HPCAT operations are supported by DOE-NNSA's Office of Experimental Sciences. The Advanced Photon Source is a U.S. Department of Energy (DOE) Office of Science User Facility operated for the DOE Office of Science by Argonne National Laboratory under Contract No. DE-AC02-06CH11357. AJC acknowledges support from EAR-2023128 for the EBSD analyses. Use of the COMPRES Cell Assembly Project was supported by COMPRES under NSF Cooperative Agreement EAR-1661511.

References

Atlas, Z. D., Dixon, J. E., Sen, G., Finny, M., & Martin-Del Pozzo, A. L. (2006). Melt inclusions from Volcán Popocatépetl and Volcán de Colima, Mexico: Melt evolution due to vapor-saturated crystallization during ascent. *Journal of Volcanology and Geothermal Research*, *153*(3–4), 221–240. https://doi.org/10.1016/j.jvolgeores.2005.06.010

Bachmann, F., Hielscher, R., & Schaeben, H. (2010). Texture analysis with MTEX–free and open source software toolbox. *Solid State Phenomena*, *160*, 63–68. https://doi.org/10.4028/www.scientific.net/ssp.160.63

Bailey, E., & Holloway, J. R. (2000). Experimental determination of elastic properties of talc to 800 C, 0.5 GPa; calculations of the effect on hydrated peridotite, and implications for cold subduction zones. *Earth and Planetary Science Letters*, *183*(3–4), 487–498. https://doi.org/10.1016/S0012-821X(00)00288-0

Bebout, G. (2013). Metasomatism in subduction zones of subducted oceanic slabs, mantle wedges, and the slab-mantle interface. In *Metasomatism and the chemical transformation of rock* (pp. 289–349). https://doi.org/10.1007/978-3-642-28394-9_9

Bebout, G. E., & Barton, M. D. (2002). Tectonic and metasomatic mixing in a high-T, subduction-zone mélange—Insights into the geochemical evolution of the slab–mantle interface. *Chemical Geology*, *187*(1–2), 79–106. https://doi.org/10.1016/S0009-2541(02)00019-0

Behr, W. M., & Smith, D. (2016). Deformation in the mantle wedge associated with Laramide flat-slab subduction. *Geochemistry, Geophysics, Geosystems*, *17*(7), 2643–2660. https://doi.org/10.1002/2016GC006361

Berman, R. G. (1988). Internally-consistent thermodynamic data for minerals in the system Na2O-K_2O-CaO-MgO-FeO-Fe_2O_3-Al_2O_3-SiO_2-TiO_2-H_2O-CO_2. *Journal of Petrology*, *29*(2), 445–522. https://doi.org/10.1093/petrology/29.2.445

Bose, K., & Ganguly, J. (1995). Experimental and theoretical studies of the stabilities of talc, antigorite and phase A at high pressures with applications to subduction processes. *Earth and Planetary Science Letters*, *136*(3–4), 109–121. https://doi.org/10.1016/0012-821X(95)00188-I

Brady, J. B. (1995). Diffusion data for silicate minerals, glasses, and liquids. *Mineral Physics and Crystallography: A Handbook of Physical Constants*, *2*, 269–290. https://doi.org/10.1029/rf002p0269

Brown, J. M., & Abramson, E. H. (2016). Elasticity of calcium and calcium-sodium amphiboles. *Physics of the Earth and Planetary Interiors*, *261*, 161–171. https://doi.org/10.1016/j.pepi.2016.10.010

Chen, P., Wang, D., Cai, N., Zhang, J., Zhang, R., & Cao, Y. (2023). Anomalous sound velocities of talc at high pressure and implications for estimating water content in mantle wedge. *Journal of Geophysical Research: Solid Earth*, *128*(11), e2023JB027309. https://doi.org/10.1029/2023JB027309

Chen, S., Guo, X., Yoshino, T., Jin, Z., & Li, P. (2018). Dehydration of phengite inferred by electrical conductivity measurements: Implication for the high conductivity anomalies relevant to the subduction zones. *Geology*, *46*(1), 11–14. https://doi.org/10.1130/G39716.1

Chen, X., Elwood Madden, A. S., & Reches, Z. E. (2017). The frictional strength of talc gouge in high-velocity shear experiments. *Journal of Geophysical Research: Solid Earth*, *122*(5), 3661–3676. https://doi.org/10.1002/2016JB013676

Codillo, E. A., Klein, F., & Marschall, H. R. (2022). Preferential Formation of chlorite over talc during Si-metasomatism of ultramafic rocks in subduction zones. *Geophysical Research Letters*, *49*(19), e2022GL100218. https://doi.org/10.1029/2022GL100218

Condit, C. B., French, M. E., Hayles, J. A., Yeung, L. Y., Chin, E. J., & Lee, C.-T. A. (2022). Rheology of metasedimentary rocks at the base of the subduction seismogenic zone. *Geochemistry, Geophysics, Geosystems*, *23*(2), e2021GC010194. https://doi.org/10.1029/2021GC010194

Dougherty, S. L., Clayton, R. W., & Helmberger, D. V. (2012). Seismic structure in central Mexico: Implications for fragmentation of the subducted Cocos plate. *Journal of Geophysical Research*, *117*(B9), B09316. https://doi.org/10.1029/2012JB009528

Egbert, G. D., Yang, B., Bedrosian, P. A., Key, K., Livelybrooks, D. W., Schultz, A., et al. (2022). Fluid transport and storage in the Cascadia forearc influenced by overriding plate lithology. *Nature Geoscience*, *15*(8), 677–682. https://doi.org/10.1038/s41561-022-00981-8

Espindola-Carmona, A., Peter, D., & Ortiz-Aleman, C. (2021). Crustal and upper-mantle structure below Central and Southern Mexico. *Journal of Geophysical Research: Solid Earth*, *126*(6), e2020JB020906. https://doi.org/10.1029/2020JB020906

Földvári, M. (2011). *Handbook of thermogravimetric system of minerals and its use in geological practice* (Vol. 213, pp. 1–180). Geological Institute of Hungary.

Fortier, S. M., & Giletti, B. J. (1991). Volume self-diffusion of oxygen in biotite, muscovite, and phlogopite micas. *Geochimica et Cosmochimica Acta*, *55*(5), 1319–1330. https://doi.org/10.1016/0016-7037(91)90310-2

Gardés, E., Gaillard, F., & Tarits, P. (2014). Toward a unified hydrous olivine electrical conductivity law. *Geochemistry, Geophysics, Geosystems*, *15*(12), 4984–5000. https://doi.org/10.1002/2014GC005496

Glover, P. W. J. (2015). Geophysical properties of the near surface Earth: Electrical properties. In *Treatise on geophysics* (2nd ed., pp. 89–137). https://doi.org/10.1016/B978-0-444-53802-4.00189-5

Grove, T. L., Till, C. B., & Krawczynski, M. J. (2012). The role of H_2O in subduction zone magmatism. *Annual Review of Earth and Planetary Sciences*, *40*(1), 413–439. https://doi.org/10.1146/annurev-earth-042711-105310

Guo, X., & Yoshino, T. (2013). Electrical conductivity of dense hydrous magnesium silicates with implication for conductivity in the stagnant slab. *Earth and Planetary Science Letters*, *369*, 239–247. https://doi.org/10.1016/j.epsl.2013.03.026

Guo, X., & Yoshino, T. (2014). Pressure-induced enhancement of proton conduction in brucite. *Geophysical Research Letters*, *41*(3), 813–819. https://doi.org/10.1002/2013GL058627

Guo, X., Yoshino, T., & Katayama, I. (2011). Electrical conductivity anisotropy of deformed talc rocks and serpentinites at 3 GPa. *Physics of the Earth and Planetary Interiors*, *188*(1–2), 69–81. https://doi.org/10.1016/j.pepi.2011.06.012

Hacker, B. R., Abers, G. A., & Peacock, S. M. (2003). Subduction Factory 1. Theoretical mineralogy, densities, seismic wave speeds, and H_2O contents. *Journal of Geophysical Research*, *108*(B1), 1–26. https://doi.org/10.1029/2001JB001127

Hao, M., Pommier, A., Codillo, E., Walter, M. J., Cross, A., Hrubiak, R., et al. (2024). Electrical conductivity and sound velocities of talc under high pressure and high temperature conditions (Version 1) [Dataset]. *Mendeley*. https://doi.org/10.17632/dk5sx5s9kh.1

Hashin, Z., & Shtrikman, S. (1962). A variational approach to the theory of the effective magnetic permeability of multiphase materials. *Journal of Applied Physics*, *33*(10), 3125–3131. https://doi.org/10.1063/1.1728579

Hirauchi, K. I., Yamamoto, Y., den Hartog, S. A., & Niemeijer, A. R. (2020). The role of metasomatic alteration on frictional properties of subduction thrusts: An example from a serpentinite body in the Franciscan Complex, California. *Earth and Planetary Science Letters*, *531*, 115967. https://doi.org/10.1016/j.epsl.2019.115967

Hrubiak, R., & Sturtevant, B. T. (2023). SonicPy: A suite of programs for ultrasound pulse-echo data acquisition and analysis. *High Pressure Research*, *43*(1), 23–39. https://doi.org/10.1080/08957959.2023.2182209

Hu, H., Dai, L., Li, H., Sun, W., & Li, B. (2018). Effect of dehydrogenation on the electrical conductivity of Fe-bearing amphibole: Implications for high conductivity anomalies in subduction zones and continental crust. *Earth and Planetary Science Letters*, *498*, 27–37. https://doi.org/10.1016/j.epsl.2018.06.003

Huebner, J. S., & Dillenburg, R. G. (1995). Impedance spectra of hot, dry silicate minerals and rock: Qualitative interpretation of spectra. *American Mineralogist*, *80*(1-2), 46–64. https://doi.org/10.2138/am-1995-1-206

Jödicke, H., Jording, A., Ferrari, L., Arzate, J., Mezger, K., & Rüpke, L. (2006). Fluid release from the subducted Cocos plate and partial melting of the crust deduced from magnetotelluric studies in southern Mexico: Implications for the generation of volcanism and subduction dynamics. *Journal of Geophysical Research*, *111*(B8), B08102. https://doi.org/10.1029/2005JB003739

Kim, Y., Clayton, R. W., Asimow, P. D., & Jackson, J. M. (2013). Generation of talc in the mantle wedge and its role in subduction dynamics in central Mexico. *Earth and Planetary Science Letters*, *384*, 81–87. https://doi.org/10.1016/j.epsl.2013.10.006

Kim, Y., Clayton, R. W., & Jackson, J. M. (2010). Geometry and seismic properties of the subducting Cocos plate in central Mexico. *Journal of Geophysical Research*, *115*(B6), B06310. https://doi.org/10.1029/2009JB006942

Kono, Y., Irifune, T., Higo, Y., Inoue, T., & Barnhoorn, A. (2010). P V T relation of MgO derived by simultaneous elastic wave velocity and in situ X-ray measurements: A new pressure scale for the mantle transition region. *Physics of the Earth and Planetary Interiors*, *183*(1–2), 196–211. https://doi.org/10.1016/j.pepi.2010.03.010

Kono, Y., Park, C., Kenney-Benson, C., Shen, G., & Wang, Y. (2014). Toward comprehensive studies of liquids at high pressures and high temperatures: Combined structure, elastic wave velocity, and viscosity measurements in the Paris–Edinburgh cell. *Physics of the Earth and Planetary Interiors*, *228*, 269–280. https://doi.org/10.1016/j.pepi.2013.09.006

Lee, J., Jung, H., Klemd, R., Tarling, M. S., & Konopelko, D. (2020). Lattice preferred orientation of talc and implications for seismic anisotropy in subduction zones. *Earth and Planetary Science Letters*, *537*, 116178. https://doi.org/10.1016/j.epsl.2020.116178

Lindquist, P. C., Condit, C. B., Hoover, W. F., Hernández-Uribe, D., & Guevara, V. E. (2023). Metasomatism and slow slip: Talc production along the flat subduction plate interface beneath Mexico (Guerrero). *Geochemistry, Geophysics, Geosystems*, *24*(8), e2023GC010981. https://doi.org/10.1029/2023GC010981

Liu, X., Currie, C. A., & Wagner, L. S. (2022). Cooling of the continental plate during flat-slab subduction. *Geosphere*, *18*(1), 49–68. https://doi.org/10.1130/GES02402.1

Mainprice, D., Le Page, Y., Rodgers, J., & Jouanna, P. (2008). Ab initio elastic properties of talc from 0 to 12 GPa: Interpretation of seismic velocities at mantle pressures and prediction of auxetic behaviour at low pressure. *Earth and Planetary Science Letters*, *274*(3–4), 327–338. https://doi.org/10.1016/j.epsl.2008.07.047

Mandler, B. E., & Grove, T. L. (2016). Controls on the stability and composition of amphibole in the Earth's mantle. *Contributions to Mineralogy and Petrology*, *171*(8–9), 1–20. https://doi.org/10.1007/s00410-016-1281-5

Manea, V. C., & Manea, M. (2011). Flat-slab thermal structure and evolution beneath central Mexico. *Pure and Applied Geophysics*, *168*(8–9), 1475–1487. https://doi.org/10.1007/s00024-010-0207-9

Manning, C. E. (1995). Phase-equilibrium controls on SiO_2 metasomatism by aqueous fluid in subduction zones: Reaction at constant pressure and temperature. *International Geology Review*, *37*(12), 1074–1093. https://doi.org/10.1080/00206819509465440

Manning, C. E. (1997). Coupled reaction and flow in subduction zones: Silica metasomatism in the mantle wedge. In *Fluid flow and transport in rocks: Mechanisms and effects* (pp. 139–148). Springer Netherlands. https://doi.org/10.1007/978-94-009-1533-6_8

Manthilake, G., Bolfan-Casanova, N., Novella, D., Mookherjee, M., & Andrault, D. (2016). Dehydration of chlorite explains anomalously high electrical conductivity in the mantle wedges. *Science Advances*, *2*(5), e1501631. https://doi.org/10.1126/sciadv.1501631

Manthilake, G., Mookherjee, M., Bolfan-Casanova, N., & Andrault, D. (2015). Electrical conductivity of lawsonite and dehydrating fluids at high pressures and temperatures. *Geophysical Research Letters*, *42*(18), 7398–7405. https://doi.org/10.1002/2015GL064804

McGary, R. S., Evans, R. L., Wannamaker, P. E., Elsenbeck, J., & Rondenay, S. (2014). Pathway from subducting slab to surface for melt and fluids beneath Mount Rainier. *Nature*, *511*(7509), 338–340. https://doi.org/10.1038/nature13493

Mierdel, K., & Keppler, H. (2004). The temperature dependence of water solubility in enstatite. *Contributions to Mineralogy and Petrology*, *148*(3), 305–311. https://doi.org/10.1007/s00410-004-0605-z

Mookherjee, M., & Mainprice, D. (2014). Unusually large shear wave anisotropy for chlorite in subduction zone settings. *Geophysical Research Letters*, *41*(5), 1506–1513. https://doi.org/10.1002/2014GL059334

Nagaya, T., Okamoto, A., Oyanagi, R., Seto, Y., Miyake, A., Uno, M., et al. (2020). Crystallographic preferred orientation of talc determined by an improved EBSD procedure for sheet silicates: Implications for anisotropy at the slab–mantle interface due to Si-metasomatism. *American Mineralogist: Journal of Earth and Planetary Materials*, *105*(6), 873–893. https://doi.org/10.2138/am-2020-7006

Ni, H., Keppler, H., & Behrens, H. (2011). Electrical conductivity of hydrous basaltic melts: Implications for partial melting in the upper mantle. *Contributions to Mineralogy and Petrology*, *162*(3), 637–650. https://doi.org/10.1007/s00410-011-0617-4

Okamoto, A., & Oyanagi, R. (2023). Si- versus Mg-metasomatism at the crust–mantle interface: Insights from experiments, natural observations and geochemical modeling. *Progress in Earth and Planetary Science*, *10*(1), 39. https://doi.org/10.1186/s40645-023-00568-w

Pardo, M., & Suárez, G. (1995). Shape of the subducted Rivera and Cocos plates in southern Mexico: Seismic and tectonic implications. *Journal of Geophysical Research*, *100*(B7), 12357–12373. https://doi.org/10.1029/95JB00919

Pawley, A. R., & Wood, B. J. (1995). The high-pressure stability of talc and 10 Å phase: Potential storage sites for H_2O in subduction zones. *American Mineralogist*, *80*(9–10), 998–1003. https://doi.org/10.2138/am-1995-9-1015

Peacock, S. M., & Wang, K. (2021). On the stability of talc in subduction zones: A possible control on the maximum depth of decoupling between the subducting plate and mantle wedge. *Geophysical Research Letters*, *48*(17), e2021GL094889. https://doi.org/10.1029/2021GL094889

Peng, Y., Mookherjee, M., Hermann, A., Manthilake, G., & Mainprice, D. (2022). Anomalous elasticity of talc at high pressures: Implications for subduction systems. *Geoscience Frontiers*, *13*(4), 101381. https://doi.org/10.1016/j.gsf.2022.101381

Plank, T., Kelley, K. A., Zimmer, M. M., Hauri, E. H., & Wallace, P. J. (2013). Why do mafic arc magmas contain ~4 wt% water on average? *Earth and Planetary Science Letters*, *364*, 168–179. https://doi.org/10.1016/j.epsl.2012.11.044

Poli, S., & Schmidt, M. W. (2002). Petrology of subducted slabs. *Annual Review of Earth and Planetary Sciences*, *30*(1), 207–235. https://doi.org/10.1146/annurev.earth.30.091201.140550

Pommier, A., & Evans, R. L. (2017). Constraints on fluids in subduction zones from electromagnetic data. *Geosphere*, *13*(4), 1026–1041. https://doi.org/10.1130/GES01473.1

Pommier, A., & Leinenweber, K. D. (2018). Electrical cell assembly for reproducible conductivity experiments in the multi-anvil. *American Mineralogist*, *103*(8), 1298–1305. https://doi.org/10.2138/am-2018-6448

Pommier, A., Williams, Q., Evans, R. L., Pal, I., & Zhang, Z. (2019). Electrical investigation of natural lawsonite and application to subduction contexts. *Journal of Geophysical Research: Solid Earth*, *124*(2), 1430–1442. https://doi.org/10.1029/2018JB016899

Sakuma, H., & Ichiki, M. (2016). Density and isothermal compressibility of supercritical H_2O–NaCl fluid: Molecular dynamics study from 673 to 2000 K, 0.2 to 2 GP a, and 0 to 22 wt% NaCl concentrations. *Geofluids*, *16*(1), 89–102. https://doi.org/10.1111/gfl.12138

Saxena, S., Pommier, A., & Tauber, M. J. (2021). Iron sulfides and anomalous electrical resistivity in cratonic environments. *Journal of Geophysical Research: Solid Earth*, *126*(9), e2021JB022297. https://doi.org/10.1029/2021JB022297

Schmidt, M., & Poli, S. (2013). Devolatilization during subduction. In *Treatise on geochemistry: vol. 4: The crust* (Vol. 4, pp. 669–701). Elsevier. https://doi.org/10.1016/B978-0-08-095975-7.00321-1

Sinmyo, R., & Keppler, H. (2017). Electrical conductivity of NaCl-bearing aqueous fluids to 600 C and 1 GPa. *Contributions to Mineralogy and Petrology*, *172*(1), 4. https://doi.org/10.1007/s00410-016-1323-z

Song, T. R. A., Helmberger, D. V., Brudzinski, M. R., Clayton, R. W., Davis, P., Pérez-Campos, X., & Singh, S. K. (2009). Subducting slab ultra-slow velocity layer coincident with silent earthquakes in southern Mexico. *Science*, *324*(5926), 502–506. https://doi.org/10.1126/science.1167595

Syracuse, E. M., van Keken, P. E., & Abers, G. A. (2010). The global range of subduction zone thermal models. *Physics of the Earth and Planetary Interiors*, *183*(1–2), 73–90. https://doi.org/10.1016/j.pepi.2010.02.004

Ulian, G., Tosoni, S., & Valdrè, G. (2014). The compressional behaviour and the mechanical properties of talc [$Mg_3Si_4O_{10}(OH)_2$]: A density functional theory investigation. *Physics and Chemistry of Minerals*, *41*(8), 639–650. https://doi.org/10.1007/s00269-014-0677-x

van Keken, P. E., & Wilson, C. R. (2023a). An introductory review of the thermal structure of subduction zones: III—Comparison between models and observations. *Progress in Earth and Planetary Science*, *10*(1), 57. https://doi.org/10.1186/s40645-023-00589-5

van Keken, P. E., & Wilson, C. R. (2023b). An introductory review of thermal structure of subduction zones: II & III [Dataset]. In *Progress in Earth and planetary science (0.9.3)*. Zenodo. https://doi.org/10.5281/zenodo.8309731

Wang, D., & Karato, S. (2013). Electrical conductivity of talc aggregates at 0.5 GPa: Influence of dehydration. *Physics and Chemistry of Minerals*, *40*(1), 11–17. https://doi.org/10.1007/s00269-012-0541-9

Wang, D., Li, H., Yi, L., Matsuzaki, T., & Yoshino, T. (2010). Anisotropy of synthetic quartz electrical conductivity at high pressure and temperature. *Journal of Geophysical Research*, *115*(B9), B09211. https://doi.org/10.1029/2009JB006695

Wang, L., Wang, D., & Shen, K. (2020). Electrical conductivity of talc dehydration at high pressures and temperatures: Implications for high-conductivity anomalies in subduction zones. *Journal of Geophysical Research: Solid Earth*, *125*(10), e2020JB020091. https://doi.org/10.1029/2020JB020091

Wilson, C. R., Spiegelman, M., van Keken, P. E., & Hacker, B. R. (2014). Fluid flow in subduction zones: The role of solid rheology and compaction pressure. *Earth and Planetary Science Letters*, *401*, 261–274. https://doi.org/10.1016/j.epsl.2014.05.052

Yi, H., Zhao, Y., Liu, Y., Wang, W., Song, S., Liu, C., et al. (2019). A novel method for surface wettability modification of talc through thermal treatment. *Applied Clay Science*, *176*, 21–28. https://doi.org/10.1016/j.clay.2019.04.023

Yoshino, T. (2010). Laboratory electrical conductivity measurement of mantle minerals. *Surveys in Geophysics*, *31*(2), 163–206. https://doi.org/10.1007/s10712-009-9084-0

Zhang, B., Yoshino, T., Wu, X., Matsuzaki, T., Shan, S., & Katsura, T. (2012). Electrical conductivity of enstatite as a function of water content: Implications for the electrical structure in the upper mantle. *Earth and Planetary Science Letters*, *357–358*, 11–20. https://doi.org/10.1016/j.epsl.2012.09.020

Zhu, M. X., Xie, H. S., Guo, J., & Xu, Z. M. (2001). An experimental study on electrical conductivity of talc at high temperature and high pressure. *Chinese Journal of Geophysics*, *44*(3), 427–434. https://doi.org/10.1002/cjg2.158